CHEMISTRY OF MATERIALS

pubs.acs.org/cm

Article

Novel Class of Rhenium Borides Based on Hexagonal Boron Networks Interconnected by Short B_2 Dumbbells

Elena Bykova,* Erik Johansson, Maxim Bykov, Stella Chariton, Hongzhan Fei, Sergey V. Ovsyannikov, Alena Aslandukova, Stefan Gabel, Hendrik Holz, Benoit Merle, Björn Alling, Igor A. Abrikosov, Jesse S. Smith, Vitali B. Prakapenka, Tomoo Katsura, Natalia Dubrovinskaia, Alexander F. Goncharov, and Leonid Dubrovinsky

Cite This: *Chem. Mater.* 2022, 34, 8138−8152

Read Online

ACCESS | Metrics & More | Article Recommendations | Supporting Information

ABSTRACT: Transition metal borides are known due to their attractive mechanical, electronic, refractive, and other properties. A new class of rhenium borides was identified by synchrotron single-crystal X-ray diffraction experiments in laser-heated diamond anvil cells between 26 and 75 GPa. Recoverable to ambient conditions, compounds rhenium triboride (ReB_3) and rhenium tetraboride (ReB_4) consist of close-packed single layers of rhenium atoms alternating with boron networks built from puckered hexagonal layers, which link short bonded (∼1.7 Å) axially oriented B_2 dumbbells. The short and incompressible Re−B and B−B bonds oriented along the hexagonal *c*-axis contribute to low axial compressibility comparable with the linear compressibility of diamond. Sub-millimeter samples of ReB_3 and ReB_4 were synthesized in a large-volume press at pressures as low as 33 GPa and used for material characterization. Crystals of both compounds are metallic and hard (Vickers hardness, H_V = 34(3) GPa). Geometrical, crystal-chemical, and theoretical analysis considerations suggest that potential ReB_x compounds with $x > 4$ can be based on the same principle of structural organization as in ReB_3 and ReB_4 and possess similar mechanical and electronic properties.

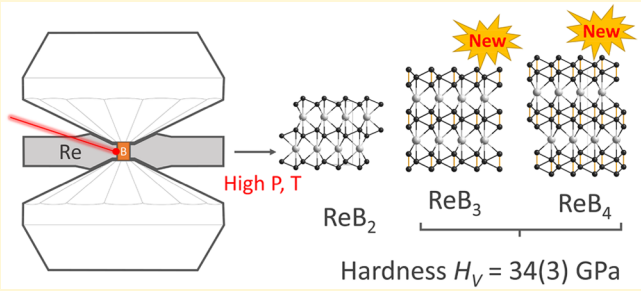

1. INTRODUCTION

Metal borides are an important class of compounds with remarkable properties such as superconductivity (MgB_2 with a T_c of 39 K[1]), low compressibility (OsB_2[2]), and very high hardness (WB_4,[3] WB_4-based solid solutions,[4] FeB_4,[5] ReB_2[6]). Therefore, synthesis of novel metal borides and investigation of their properties are of great interest for materials science and engineering.

Transition metal borides with a metal boron ratio ≥ 2 are often considered as potential candidates for hard and incompressible materials.[7] The crystal structures of diborides are generally based on alternating hexagonal metallic and boron layers where the latter can be flat (AlB_2 type) or buckled (ReB_2 and OsB_2 types).[7,8] Further enrichment with boron results in the formation of 3D boron networks (for example, CrB_4, MnB_4, FeB_4) or frameworks built from interconnected boron clusters (for example, YB_4 and CaB_6 types formed by B_6 octahedra; AlB_{12} and YB_{66} type; metal-doped α- and β-B, all formed by B_{12} icosahedra) where metal atoms fill appropriate voids.[7,8] Strong covalent boron−boron and often metal−boron bonds contribute to exceptional mechanical properties. Among these compounds, one of the most studied is, perhaps, rhenium diboride, ReB_2. Its potential superhardness ignites hot debates. Chung et al.[6] determined that mechanical properties of ReB_2 were anisotropic, and its Vickers hardness (H_V) varied from 30.1(1.30) to 48.0(5.6) GPa depending on the indentation load,[6] which brought (for very low load indentations) ReB_2 to the class of superhard materials such as diamond (70 to 100 GPa) and cubic boron nitride (45 to 50 GPa). Theoretical calculations suggested hardness values from 40 to 44 GPa.[9−12] However, the later experimental study based on measurements of elastic moduli (by an ultrasonic method) and microhardness casted doubts on the superhardness of ReB_2 and suggested more moderate values of H_V (about 22 GPa[13]). Levine et al.[14] reported that H_V and other mechanical properties strongly depend on the morphology of the samples and on the presence of an excess of boron, with a single-crystalline sample showing a much higher value of H_V (39.5(2.5) GPa) than randomly oriented polycrystalline material (27.0(4.7) GPa).

Received: February 17, 2022
Revised: July 23, 2022
Published: September 6, 2022

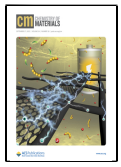

ACS Publications

© 2022 The Authors. Published by American Chemical Society

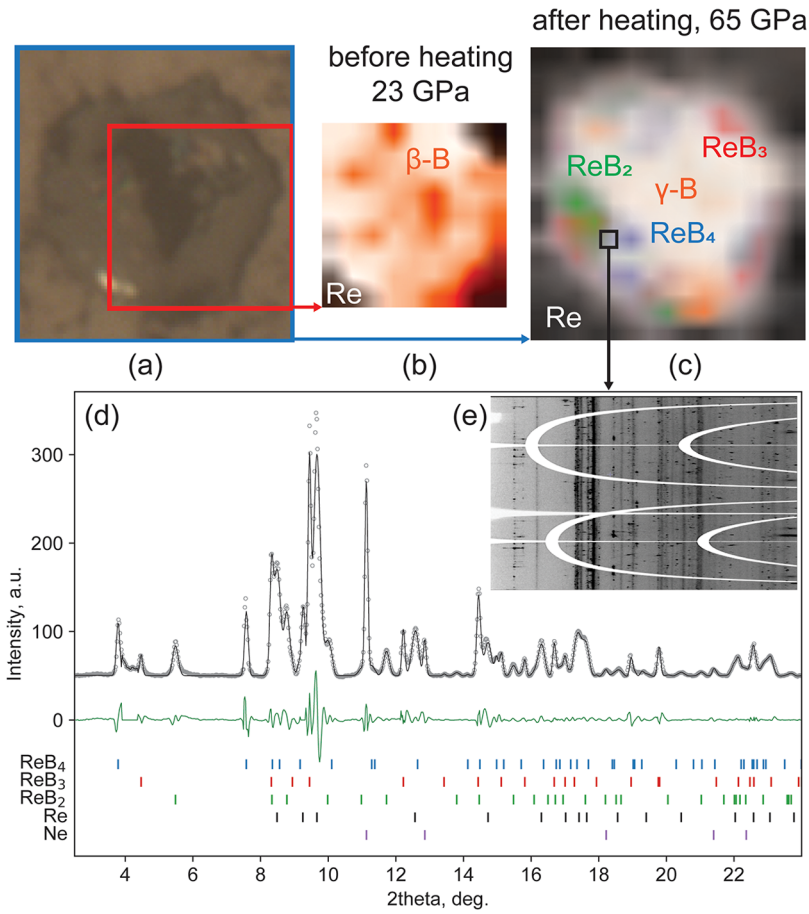

Figure 1. Microphotograph of the sample chamber at a loading pressure of 23 GPa (a) with corresponding phase distributions (b) and a phase map at 65 GPa after all laser heating cycles (c). By using a combination of powder and single-crystal XRD methods, three borides of rhenium were identified in the pressure chamber, ReB_2, ReB_3, and ReB_4. Black box in (c) shows the position where all three phases coexist; therefore this point was selected for X-ray diffraction data collection under stepwise pressure release. The lower image (d) shows an example of such powder diffraction data collected at 65 GPa (λ = 0.344 53 Å): experimental data, gray circles; Le Bail fit, black solid lines; difference curves, green solid lines; ticks show predicted positions of the diffraction peaks. The sample exhibits significant non-hydrostaticity, as can be seen from a pronounced curvature of diffraction lines in the unrolled image (inset, e; white stripes correspond to masked areas).

Rhenium borides with boron contents higher than in ReB_2 have never been obtained experimentally, although theoretical studies have suggested that they may have mechanical properties similar to ReB_2. Rhenium triboride, ReB_3, first claimed to be synthesized in 1960,[15] later appeared to be ReB_2.[16] Theoretical studies suggested[17,18] that ReB_3 should have $P\bar{6}m2$ symmetry and a Vickers hardness of 29−30 GPa. The predicted crystal structure consisted of flat hexagonal layers of rhenium atoms alternating with buckled hexagonal networks formed by boron atoms.

It was proposed that rhenium tetraboride, ReB_4, should adopt the crystal structure of superhard WB_4 (sp. gr. $P6_3/mmc$), resulting in an expected hardness of 50.3 GPa.[19] However, later calculations suggested positive formation enthalpy and $R\bar{3}m$[20,21] or $C2/m$[17] symmetry for ReB_4. The values of bulk and shear moduli provided in these papers imply a H_V of 30−33 GPa for this phase.

Despite a vast number of theoretical studies on rhenium borides, many inconsistencies in their possible crystal structures, chemical compositions, stability fields, and mechanical properties still remain. Here we have applied methods of single-crystal X-ray diffraction in laser-heated diamond anvil cells (DACs) in order to demonstrably synthesize two novel boron-rich borides of rhenium, ReB_3 and ReB_4, and characterize their crystal structure and compression behavior. We discuss their structural, mechanical, and electronic properties derived from theoretical and experimental methods and compare them with the literature data. The structural organization of ReB_3 and ReB_4 allows us to propose a new class of rhenium borides that can be stabilized by high pressure.

2. EXPERIMENTAL SECTION

2.1. Sample Preparation. As a boron source we used a single crystal of β-boron synthesized from amorphous boron at 3.0 GPa and 1500 °C in a piston−cylinder apparatus according to a procedure described in ref 22.

A dark red single crystal of β-boron with dimensions of 0.05 × 0.05 × 0.02 mm^3 and a small ruby sphere (for pressure estimation) were loaded into a mini-BX90 membrane-driven type DAC[23] equipped with Boehler−Almax diamonds with a 200 μm culet size (see Figure 1a,b). A hole with a diameter of about 100 μm in a rhenium gasket preindented to 25 μm thickness served as a pressure chamber. The gasket (99.99% purity) was used as a source of rhenium. Neon was used both as a pressure-transmitting medium and as a pressure standard.[24] After the gas loading, boron almost fully filled the pressure chamber; it resulted in significant non-hydrostatic stresses across the sample during the experiment (Figure 1e).

https://doi.org/10.1021/acs.chemmater.2c00520
Chem. Mater. 2022, 34, 8138−8152

2.2. Laser Heating Experiments. The DAC connected to a gas membrane was compressed stepwise to a maximum pressure of 75.0(5) GPa and laser-heated around 26, 47, and 64 GPa to a maximum temperature of 3000 K (see Table S1 for a detailed summary of the experiments; positions in the pressure chamber where laser heating procedures were performed are shown in Figure S1). After each laser heating cycle, a detailed X-ray diffraction (XRD) map was collected around the heated spot in order to determine the phase composition of the reaction product. At each pressure point, single-crystal XRD images were collected in one or two spots with decent quality of the diffraction data in order to determine the phase composition of the reaction product. The single-crystal XRD images were recorded while rotating the sample about a single ω-axis from −30° to +30° in small steps of 0.5°.

The laser heating coupled with XRD measurements was conducted at the 13-IDD beamline at the Advanced Photon Source (APS), Chicago, USA (Pilatus CdTe 1M detector, λ = 0.295 20 Å, KB-mirror focusing).[25] Lasers were focused down to about 20 μm in diameter (full width at half-maximum). The surface temperature was measured by the standard spectroradiometry method[26] using an IsoPlane SCT 320 spectrometer with a PI-MAX4 1024i ICCD camera from Princeton Instruments.

2.3. Decompression Experiments. After the laser heating experiments the DAC was disconnected from the membrane, causing the pressure to drop gradually from 75 GPa to 65 GPa by itself, and powder diffraction images were collected concurrently every 1 GPa. Then the DAC was transferred to the 16-ID-B beamline at APS (Pilatus Si 1M detector, λ = 0.344 53 Å, KB-mirror focusing), where it was manually decompressed in nine steps to an ambient pressure with single-crystal XRD being collected at the each pressure point (the black box in Figure 1c corresponds to the position in the pressure chamber where diffraction data were measured).

2.4. XRD Data Processing. DIOPTAS software[27] was used for phase analysis and calculation of pressures from the positions of the XRD lines of Ne. Two-dimensional XRD maps were analyzed using XDI software.[28] Sample-to-detector distance, coordinates of the beam center, tilt angle, and tilt plane rotation angle of the detector images were calibrated using LaB_6 (13-ID-D experiments) or CeO_2 (16-ID-B experiments) powders.

Laser heating at high pressures always resulted in multicomponent and multigrain samples. Phase analysis was performed by comparing experimental powder XRD patterns and the calculated positions of the reflections belonging to known phases (such as Re, Ne, ReB_2, β-B, γ-B). When unexpected reflections appeared, we used corresponding single-crystal XRD data sets to determine the crystal structures of the unknown phase(s). Additionally, the powder XRD patterns collected on decompression were analyzed in JANA2020, where the unit cell parameters of the phases in the multiphase mixtures were refined from a full-profile Le Bail fit.[29]

Single-crystal XRD data (unit cell determination, integration of the reflection intensities, empirical absorption correction) were processed using CrysAlisPro software.[30] By careful visual analysis of the reciprocal space with Ewald Explorer (implemented in CrysAlisPro), we manually selected about 30 reflections, followed a 3D-lattice pattern, and searched a unit cell on these reflections. The found unit cell was refined on the whole set of reflections with 0.05 tolerance (maximum allowed displacement of the h, k, l indices from integer) and used for further data integration.

A single crystal of orthoenstatite ($(Mg_{1.93},Fe_{0.06})(Si_{1.93},Al_{0.06})O_6$, *Pbca*, a = 18.2391(3), b = 8.8117(2), c = 5.18320(10) Å) was used to calibrate the instrument model of CrysAlisPro (the sample-to-detector distance, the detector's origin, offsets of the goniometer angles, rotation of the X-ray beam and the detector around the instrument axis).

2.5. Structure Solution and Refinement. The analysis of the unit cell parameters obtained from various grains in the single-crystal XRD data sets allowed us to identify two novel borides of rhenium, namely, ReB_3 and ReB_4. The structures were determined by SHELXT,[31] a structure solution program that uses the method of intrinsic phasing. The crystal structure was refined against F^2 on all data by full-matrix least-squares with the SHELXL[32] software. SHELXT and SHELXL programs were implemented in the Olex2 software package.[33]

In both structures, only z-coordinates of boron atoms, thermal parameters, and scale factors have to be included in the refinements. Since the body of the diamond anvil cell shadows more than 50% of the diffraction reflections, the reflection data sets were incomplete. In order to improve the data/parameter ratio, only atomic thermal parameters of rhenium were refined in anisotropic approximation. For both borides, the resulting R_1 varied from 2% to 5%. Due to the presence of high-Z rhenium atoms, the residual electron density peaks were on the order of 2−6 e/Å^3, which is comparable with the number of electrons in boron atoms. Nevertheless, the assignment of the residual density peaks to boron atoms did not improve the final R-values, and therefore, the high residuals likely originate from incompleteness of the XRD data sets. The typical data/parameter ratios were on the order of 6−10. The detailed summary of the crystal structure refinements along with unit cell parameters, atomic coordinates, and isotropic displacement parameters is shown in Tables S2 and S3.

2.6. Scale-up Synthesis in a Large-Volume Press. Several high-pressure high-temperature synthesis runs at 20−23 GPa were performed using multianvil presses at Bayerisches Geoinstitut (Bayreuth). For the syntheses, we used amorphous boron (95−97% purity) and either rhenium powder (99.99% purity) or rhenium foil. The pressure−temperature conditions are listed in Table S1. The samples were kept at target temperatures for 24 h. We used standard assemblies, including an octahedron container, $LaCrO_3$ heater, rhenium sample capsules, MgO insulating cylinders separating the sample capsule from the heater, and a W3Re/W25Re thermocouple for temperature determination. Further details of these HP-HT syntheses can be found in earlier publications.[34,35]

High-pressure synthesis experiments at 33 GPa were performed using the 15-MN multianvil press (IRIS15) installed at the Bayerisches Geoinstitut.[36] The boron powder was loaded into Re capsules, which also acted as the heater. The capsules were placed in a ZrO_2 thermal insulator within a Cr_2O_3-doped MgO octahedron with 5.7 mm edge lengths. A W/Re (D-type) thermocouple whose junction was placed between the two capsules was used to monitor the temperature. The whole cell assembly was compressed to a pressure of 33 GPa at room temperature using eight pieces of tungsten carbide cubes with 1.5 mm truncation edge lengths, followed by heating to a temperature of 1700 °C with a ramping rate of ∼100 °C/min. After keeping at the target temperature for 5 h, the assembly was quenched to room temperature by switching off the power supply and decompressed to ambient conditions over a duration of 15 h.

2.7. Scanning Electron Microscopy. The capsule retrieved from the synthesis at 33 GPa was cut crosswise and polished with diamond disc pads. The chemical composition and morphology of the synthesized sample (Figure S2) were studied by means of scanning electron microscopy (Zeiss SEM, Leo Gemini 1530 with a Schottky field emission gun employing an accelerating voltage of 15−20 kV).

2.8. Hardness Measurements. According to XRD studies, ReB_3 and ReB_4 are always found together, and it did not prove possible to separate these phases between individual particles with sufficient sizes for reliable hardness measurements. Therefore, we used the polished part of the capsule retrieved from the synthesis at 33 GPa for these studies (Figure S3).

Nanoindentation was performed using a Nanoindenter G200 platform (KLA-Tencor, Milpitas, CA, USA), equipped with a Berkovich diamond tip (Synton MDP, Nidau, Switzerland) and featuring the continuous stiffness method (CSM).[37] The sample was indented at six different locations separated by a distance of at least 30 μm, so that their plastic zones did not overlap; see Figure S3. For each measurement, loading was performed at a constant strain rate of 0.025 s^{-1} up to a maximal indentation depth of at least 800 nm. A 2 nm large CSM oscillation superimposed at 41 Hz on the loading signal was used to continuously measure the hardness and Young's modulus with increasing indentation depth. The acquired data were evaluated using the Oliver−Pharr method.[38,39] To this purpose, the diamond

https://doi.org/10.1021/acs.chemmater.2c00520
Chem. Mater. 2022, 34, 8138−8152

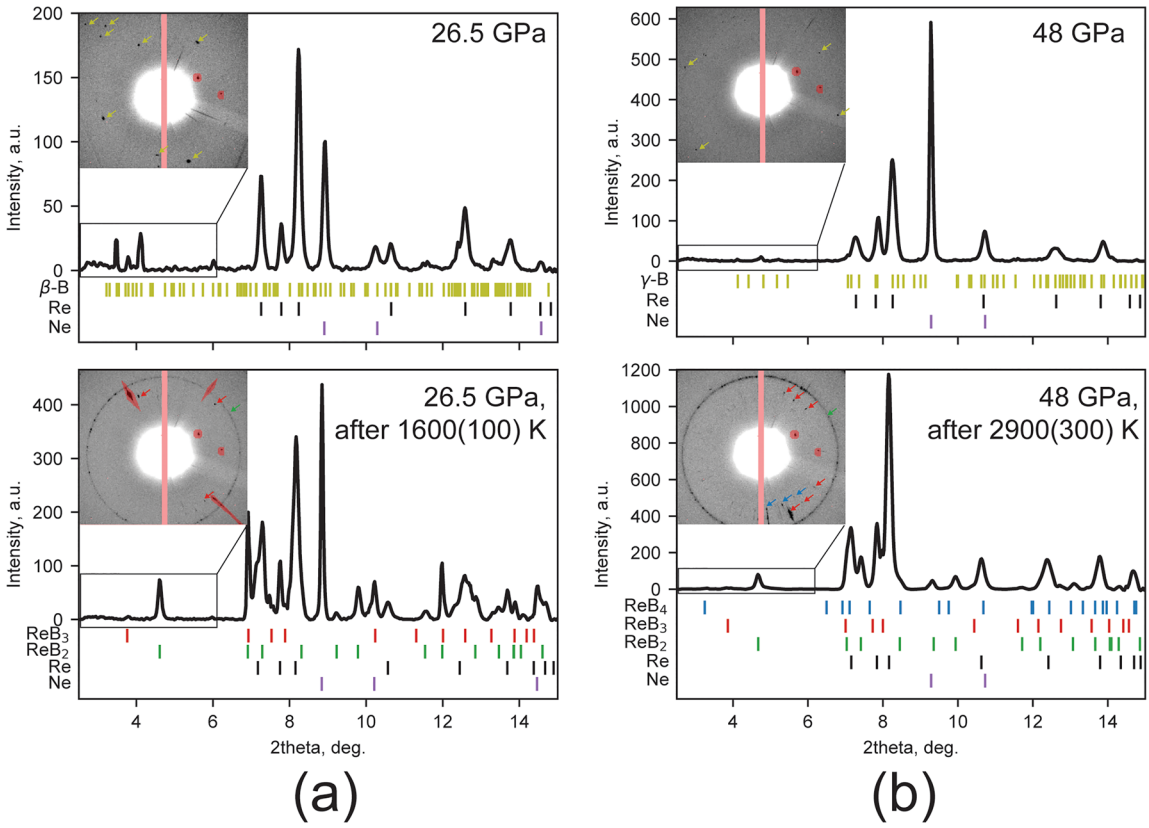

Figure 2. Synthesis of ReB_3 and ReB_4 at high-pressure and high-temperature conditions. Powder XRD profiles before and after heating showing emergence of diffraction peaks belonging to new borides: (a) ReB_3 at 26.5 GPa and (*b*) ReB_3 and ReB_4 at 48 GPa. Ticks below the profiles correspond to the phases observed in the spot. Insets show fragments of corresponding 2D diffraction images at the low-2θ region with arrows pointing out peaks belonging to β-B, γ-B (both, olive color), ReB_2 (green), ReB_3 (red), and ReB_4 (blue). Diffuse scattering lines belonging to ReB_3 and two detector glitches are masked.

punch geometry was calibrated up to 2500 nm in fused silica, and the machine frame stiffness correction was refined so as to obtain a constant stiffness-squared-overload ratio during indentation on the samples. The conversion of the reduced moduli to Young's moduli was performed assuming a Poisson's ratio of 0.21 for ReB_3/ReB_4. The mechanical properties were averaged over the indentation depth range 200−300 nm in order to minimize both effects of tip blunting (at shallow depth) and crack formation inside the capsule material (at large depth).

2.9. Electrical Resistance. For the reasons described above, we used a sample containing both ReB_3 and ReB_4 (dimensions 120 × 100 × 70 μm^3) for collecting resistance data as a function of temperature. The electrical resistance was measured by the four-probe method passing a constant DC 90 mA current through the sample and measuring both current and voltage drop across the sample. The temperature was measured using an S-type thermocouple. The electrical resistance grows with increasing temperature from 225 K to 350 K, typical for a metal (Figure S4).

2.10. Theoretical Calculations. First-principles calculations in the framework of density functional theory (DFT),[40−43] as implemented in the Vienna Ab initio Simulation Package (VASP),[44,45] have been used to derive electronic and phonon properties in ReB_x (x = 2−7) structures.

The projector-augmented-wave (PAW) method[46] has been employed to expand the electronic wave function in plane waves. The generalized gradient approximation (GGA) functional as proposed by Perdew, Burke, and Ernzerhof (PBE96)[47] has been used for calculating the exchange−correlation energies. To ensure a sufficient energy and force convergence, we have set the plane-wave energy cutoff to 600 eV. For the electronic structure calculations we have sampled the Brillouin zone of ReB_x using a 15 × 15 × 15 k-point mesh in the Monkhorst−Pack scheme,[48] and a 5 × 5 × 5 k-point mesh has been used for a 4 × 4 × 4 supercell of ReB_3 (256 atoms) and 3 × 3 × 3 supercell of ReB_4 (270 atoms) in phonon calculations.

The small displacement method, as implemented in PHONOPY,[49] has been employed to calculate phonon frequencies and band structures, using a 21 × 21 × 21 q-point mesh. Atomic displacements of 0.01 Å from their equilibrium positions have been performed for a symmetry-reduced set of displacements, using the Parlinski−Li−Kawazoe method.[50]

Equilibrium volumes and bulk moduli have been obtained by fitting energy−volume curves using the third-order Birch−Murnaghan equation of state.[51−53]

Electronic density of states (DOS) has been calculated using the tetrahedron method with Blöchl corrections[54] for Brillouin-zone integrations, with settings similar to those when fully relaxing the structures.

Elastic constants have been calculated by straining fully relaxed unit cells with ±1% and ±2% distortions, fixing the cell volume, and then fitting the total energy to a second-order Taylor expansion.[55−58] For all the ReB_x structures, five independent elastic constants have been calculated to complete the elastic tensor, namely, c_{11}, c_{12}, c_{13}, c_{33}, and c_{44}. We have found that a k-point mesh of 27 × 27 × 27 and an energy cutoff of 600 eV have given converged elastic constants that satisfy the Born stability criteria.[59]

3. RESULTS AND DISCUSSION

3.1. Synthesis of High-Pressure Borides. After the low-temperature laser heating (below 1000 K), β-boron was already transformed to polycrystalline γ-B. At 26.5(5) GPa after heating to about 1600(100) K, we observed the appearance of the new reflections that were lately identified as single-crystal ReB_3 coexisting with fine-powdered ReB_2

https://doi.org/10.1021/acs.chemmater.2c00520
Chem. Mater. 2022, 34, 8138−8152

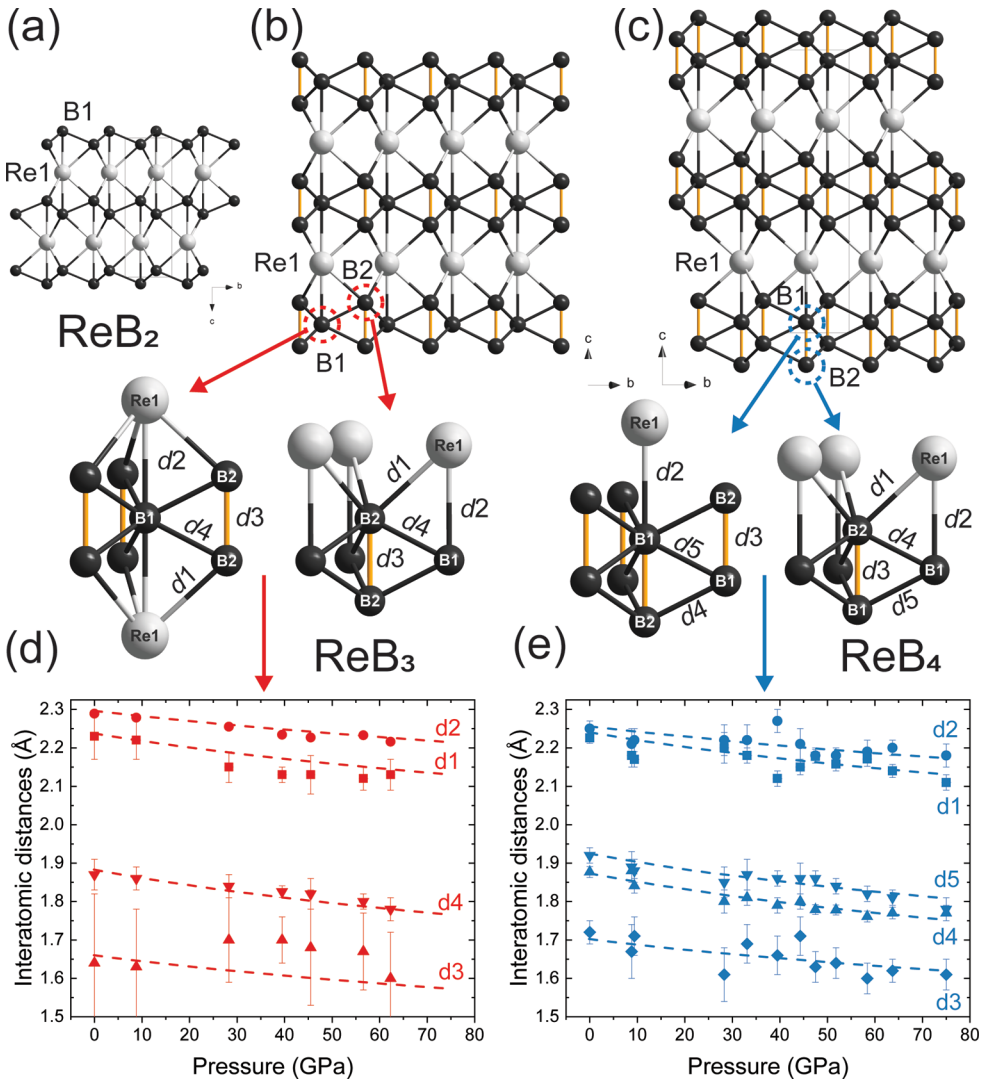

Figure 3. Crystal structures of the rhenium borides synthesized in the current work: ReB_2 (a); ReB_3 (b); ReB_4 (c). All structures consist of hexagonal layers of Re atoms (gray spheres) interchanging with a network formed by covalently bonded boron atoms (black spheres). Unlike ReB_2, triborides and tetraborides of rhenium possess short B−B distances oriented along the *c*-axis (highlighted with orange color). Insets show coordination of individual boron atoms. Compressibility of interatomic distances and bonds in ReB_3 (red, d) and ReB_4 (blue, e): *d*1, *d*2, Re···B distances; *d*3−*d*5, B···B bonds. Solid symbols are data retrieved from single-crystal X-ray diffraction measurements; dash lines correspond to the values computed by DFT.

(Figure 2a). At higher pressure (46−48 GPa), we started seeing the appearance of spots belonging to another novel rhenium boride, ReB_4, after heating above 2600(200) K (Figure 2b). At these conditions, ReB_4 was found together with ReB_2 and ReB_3. At 63−65 GPa, heating of γ-B and Re above ca. 2000 K resulted in a mixture of ReB_2 and ReB_3, and at 2450(200) K, ReB_2, ReB_3, and ReB_4. Interestingly, on heating γ-B and Re to even higher temperatures (2600(400) K) a mixture of only ReB_2 and ReB_4 was observed, suggesting that ReB_3 forms at intermediate temperatures and ReB_4 at higher ones (Figure S1b).

Following laser heating experiments, we performed several attempts to scale up the synthesis in a large-volume apparatus. Below 23 GPa and 2000 K only ReB_2 and Re_7B_3 could be synthesized. In a synthesis at higher pressures and temperatures (33 GPa, 2073−2123 K) both ReB_3 and ReB_4 were found (Figure S2). Thus, we estimate that the lowest limit for synthesis of ReB_3 is about 26−27 and 33 GPa for ReB_4 (Figure S1b).

3.2. Crystal Structure and Compressibility of ReB_3 and ReB_4. ReB_3 crystallizes in a hexagonal crystal structure (sp. gr. $P\bar{6}m2$, Z = 1), as predicted earlier by theoretical calculations.[17,18] All atoms are located on special positions: the Re1 atom occupies Wycoff position 1*a* (0, 0, 0), B1 occupies 1*b* (0, 0, 0.5), and B2 is located on 2*h* (1/3, 2/3, *z*).

ReB_4 adopts a hexagonal crystal structure (sp. gr. $P6_3/mmc$, Z = 2) different from the WB_4 type,[19] which also has $P6_3/mmc$ symmetry. All atoms in ReB_4 are located on special positions: the Re1 atom occupies Wycoff position 2*d* (2/3, 1/3, 1/4), B1 occupies 4*f* (1/3, 2/3, *z*), and B2 is located on 4*f* (1/3, 2/3, *z*). The determined structure was not considered in previous theoretical calculations for ReB_4; nevertheless it was predicted for MoB_4.[60] No phase transitions were observed in ReB_3 and ReB_4 until the highest studied pressure (75 GPa).

Crystal structures of all boron-rich rhenium borides, ReB_x (x = 2−4), share many similarities (see Figure 3a,b,c, respectively). They are composed of hexagonal layers of Re atoms interchanging with a network formed by covalently

https://doi.org/10.1021/acs.chemmater.2c00520
Chem. Mater. 2022, 34, 8138−8152

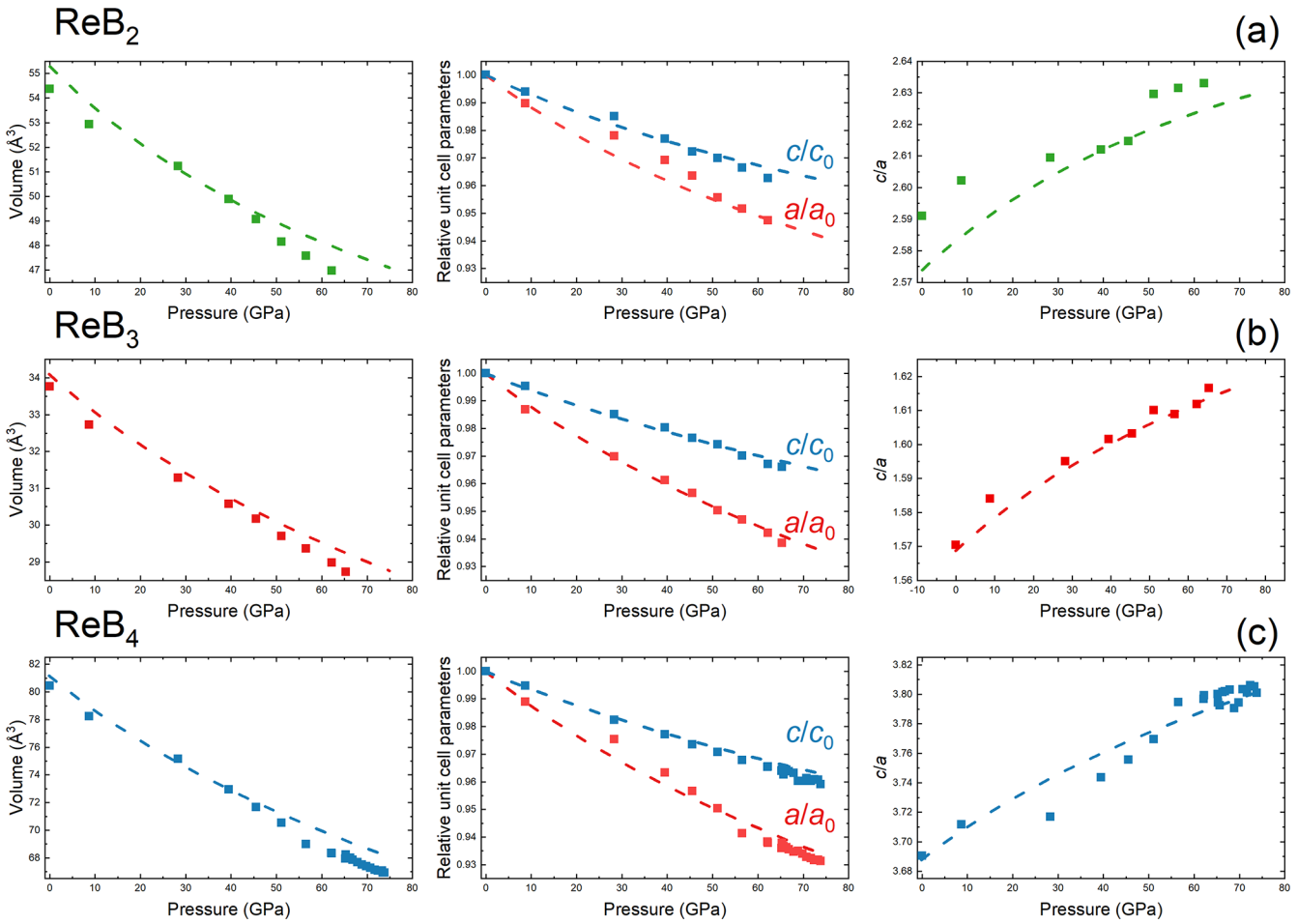

Figure 4. Unit cell volume, relative unit cell parameters, and c/a ratio of rhenium borides studied in the current work as a function of pressure: ReB_2 (a); ReB_3 (b); ReB_4 (c). Solid filled symbols represent experimental data; dashed lines correspond to the values computed by DFT.

bonded boron atoms. In the simplest case, the ReB_2 boron network is organized as a one-dimensional layer formed by condensed six-membered rings in a chairlike conformation. Similar layers can be found in gray arsenic (A7 type) and high-pressure modification of black phosphorus.[61] In order to obtain the structure of ReB_3, half of the boron atoms of such a network should be arranged by additional boron atoms that form B_2 dumbbells oriented along the c-axis. The B−B distances in the dumbbells are found to be the shortest ones in the structure (about 1.66 Å at ambient pressure). In ReB_4, all atoms are arranged by such short dumbbells: the boron network appears as double-layered chairlike sheets. Notably, in metal diborides with an AlB_2-type structure (dominant structure type in diborides) where metal atoms are sandwiched between flat graphene-like sheets $[B_n]^-$, the coordination number of metal atoms is 12. Due to the chairlike conformation of boron rings in rhenium borides, the coordination number is decreased to 8.

In the crystal structures of ReB_3 and ReB_4, since atoms occupy highly symmetric special positions, only coordinate z of some boron has to be refined; therefore only these few values fully derive the set of the interatomic distances in the corresponding structure. The significant differences between scattering factors of rhenium and boron atoms result in large uncertainties of determination of boron positions and pronounced variations in interatomic Re−B and B−B distances (Figure 3d,e). Nevertheless, the above distances agree with those obtained from theoretical calculations within the experimental uncertainties. Calculations suggest that the lowest compressibility has a Re−B1 ($d2$ at Figure 3) distance oriented along the c-axis, then come Re−B2 ($d1$) and the shortest distance in boron dumbbells ($d3$) with a similar compressibility, while the most compressible ones are the longer distances in the boron network ($d4$, $d5$).

To obtain unit cell volumes and axial compressibilities, one needs accurate lattice parameters at various pressures. In the current work, we collected both single-crystal and powder XRD data during the decompression. The studied sample had multiple fine single-crystal grains. Due to large stresses, the variation of unit cell volumes derived from various grains by the single-crystal diffraction reaches 3%, preventing accurate fits to an equation of state. In order to address this problem, we used powder XRD data to get "averaged" unit cell parameters over all grains. For a better comparison of the unit cell volumes and axial compressibilities among the observed borides, we selected a point on a sample where all three phases (ReB_2, ReB_3, and ReB_4) coexisted, and we performed Le Bail refinement of the corresponding powder profiles (Figure 1c,d). The experimental values agree well with those obtained by theoretical calculations (Figure 4). At ambient conditions, the unit cell parameters determined in such a way are as follows: ReB_3, a_0 = 2.9172(3) Å, c_0 = 4.5809(8) Å, V_0 = 33.760(8) Å^3; ReB_4, a_0 = 2.9305(2) Å, c_0 = 10.8148(14) Å, V_0 = 80.434(12) Å^3.

https://doi.org/10.1021/acs.chemmater.2c00520
Chem. Mater. 2022, 34, 8138−8152

Table 1. Parameters of the Birch–Murnaghan Equation of State of Rhenium Borides Characterized in the Current Work along with Literature Values: Volume V_0, Bulk Modulus B_0, and Its Pressure Derivative B_0' at Ambient Conditions[a]

		V_0 (Å^3), exptl	V_0 (Å^3)	B_0 (GPa)	B_0'	ref
ReB_2	expt	54.37(2)	54.4(2)	333(15)	4 (fixed)	this work
	0–65 GPa					
	DFT-GGA		55.34	331.0	4.12	this work
	expt		54.53	364	3.53	ref 62
	35–241 GPa					
ReB_3	expt	33.760(8)	33.76(2)	353(17)	2.2(6)	this work
	0–65 GPa		33.76(3)	306(5)	4 (fixed)	
	DFT-GGA		34.10	310.6	4.07	this work
	DFT-GGA			320	N/A	ref 18
ReB_4	expt	80.434(12)	80.5(3)	366(24)	1.4(4)	this work
	0–75 GPa		80.43(fixed)	281(4)	4 (fixed)	
	DFT-GGA		81.17	301.9	3.92	this work
ReB_5	DFT-GGA		47.06	285.8	3.99	this work
ReB_6	DFT-GGA		106.88	283.6	3.91	this work
ReB_7	DFT-GGA		59.98	270.5	4.00	this work

[a]Experimental unit cell volumes V_0 of ReB_x (x = 2–4) were derived by La Bail fit of corresponding powder XRD profiles.

A pronounced change in volume compressibility appears between 40 and 50 GPa, above which all borides seem to become more compressible. Such behavior was observed above 35 GPa in ReB_2 and explained by a change from uniaxial to non-hydrostatic compression.[62] When fitting with the single third-order Birch–Murnaghan equation of state (EoS), this resulted in a significant deviation of B_0' from the canonical value of 4 and consequently overestimated values of bulk moduli, B_0 (Table 1). The fit with the second order EoS (when B_0' is fixed to 4) gives similar values of the bulk moduli (333, 306, and 281 GPa for ReB_2, ReB_3, and ReB_4, respectively), which corresponds well with behavior of V/V_0 ratios for all three borides (Figure S5). Nevertheless, in the row $ReB_2 \rightarrow ReB_3 \rightarrow ReB_4$, there is a noticeable tendency for the bulk moduli to decrease with increasing boron content.

Anisotropy in the bond compressibility, where the least compressible bonds are preferably oriented along the c-direction (Re–B1 ($d2$) and B–B distances in dumbbells ($d3$)), agrees with the anisotropy in the unit cell parameters where parameter a is more compressible than c. Both parameters become more compressible with increasing boron content (Figure 3). This anisotropy can be seen in the calculated values of the elastic tensor of ReB_x (x = 2–4) (Table 2) where c_{33} is 50–75% higher than c_{11}. All compounds have high c_{33}, especially for ReB_2 and ReB_4, where c_{33} (1010 and 999 GPa, respectively) becomes comparable to c_{11} of diamond (1078 GPa[70]).

3.3. Stability of the ReB_3 and ReB_4 and Possible Existence of Borides with Higher Boron Content. The structural similarities of boron-rich borides suggest that they form a homologous series and that other more complex borides based on the similar principle of atomic organization can exist. Having the first three members of such series, we can suggest the following tentative recipe for generating structures of borides with higher boron content. When staring with the parent ReB_2 structure (sp. gr. $P6_3/mmc$), one can obtain ReB_3 by adding a boron atom to the groove in the chairlike boron network (Figure S6) so that the formed short B–B bond orients parallel to the c-axis. Every second layer of the Re hcp network has to move by $-1/3a + 1/3b$ to match the new geometry of the B-network. At ambient pressure, the addition of a single boron atom to the chemical formula increases the c parameter by 1.66 Å (approximate length of the B_2 dumbbell), whereas the a and b parameters remain nearly unchanged (Table S4). Borides with even numbers of boron atoms in the chemical formula will crystallize in the $P6_3/mmc$ space group, while ones with odd numbers of atoms will have the space group $P\bar{6}m2$. The unit cell parameters and atomic coordinates for ReB_x with x = 5–7 constructed by this principle (after geometry optimization with DFT) are given in Table S4.

We performed theoretical calculations to determine the relative stability of the ReB_x (x = 2–7) phases. For all the studied borides, except the ReB_7, we found no imaginary frequencies at the phonon dispersion curves, suggesting their dynamical stability at ambient pressure (Figure 5). As shown in Figure 6, the borides with higher boron contents tend to become thermodynamically stable at higher pressures. In good agreement with the experimental data, ReB_3 becomes stable above 25 GPa. Theory significantly overestimated the stability pressure for ReB_4 (above 92 GPa vs 33 GPa in the experiment); however ReB_4 is located just 25 meV/atom above the convex hull already at 30 GPa. The high temperatures applied in the experiments probably allowed overcoming this barrier and stabilizing metastable ReB_4, while ReB_5 (sp. gr. $P\bar{6}m2$), ReB_6 (sp. gr. $P6_3/mmc$), and ReB_7 (sp. gr. $P\bar{6}m2$) remain above the convex hull to at least 200 GPa.

Structure types of ReB_x (x = 2–4) were observed in other transition metal borides. The crystal structure of ReB_4 (sp. gr. $P6_3/mmc$) was found earlier in MoB_4 and also proposed as a ground state for IrB_4[71] and RuB_4.[72] The crystal structure of ReB_3 (sp. gr. $P\bar{6}m2$) was proposed as a stable phase for WB_3.[73] Since the atomic radii of 4d and 5d metals of groups VI–IX are similar, one should not exclude the possibility that the extended hexagonal boron networks can exist or be stabilized in other transition metal borides at extreme conditions.

The fact that higher borides ReB_x (x > 2) become thermodynamically stable at high pressures is particularly interesting, because compression promotes the boron network to "grow" further in the c-direction by connecting single puckered hexagonal boron layers through short B–B bonds: starting from single-layer boron sheets in ReB_2, via a shared-corners $1^1/_2$ layer in ReB_3, to double layers in ReB_4 and triple layers in ReB_6, etc. (Figure S6). Further growth would end up at an imaginary boron polymorph (we denote it as $hP6$-B) that

https://doi.org/10.1021/acs.chemmater.2c00520
Chem. Mater. 2022, 34, 8138–8152

Table 2. Calculated Elastic Tensor Constants c_{ij}, Isotropic Bulk Modulus B, Shear Modulus G, Young's Modulus E (all units in GPa), Poisson's Ratio (σ), and Estimated Values of Vickers Hardness H_V (GPa) of ReB_x (x = 2−7) Compared with Available Literature Values on Rhenium Borides,[6,9−14,17,18,20,21,63,64] Rhenium,[65] and γ-B.[66−68a]

composition	sp. gr.		c_{11}	c_{12}	c_{13}	c_{33}	c_{44}	c_{66}	B	G	B/G	E	σ	H_V	ref
Re	$P6_3/mmc$	calc+exp	591	361	203	793	162	115	390	168	2.32	441	0.31	12.0	65
Re_3B	$Cmcm$	calc							380	151	2.50	402	0.32	9.8	17
	$Cmcm$	calc							327						63
	$Cmcm$	expt							393(3)						63
	$C2/m$	calc							371(1)	150	2.47	397	0.32	10.0	63
	$C2/m$	expt							390(3)					11	63
Re_7B_3	$P6_3mc$	calc							378	160	2.36	421	0.31	11.2	64
	$P6_3mc$	calc	603	268	273	590	133	168	380	152	2.50	403	0.32	9.9	17
	$P6_3mc$	calc							381(1)	148	2.57	393	0.33	9.3	63
	$P6_3mc$	expt							391(5)					14(1)	63
Re_2B	$Pbnm$	calc							367	216	1.70	542	0.25	22.0	64
Re_2B	$P2_1/m$	calc							378	188	2.01	483	0.29	15.9	17
Re_2B	$C2/m$	calc							393	210	1.87	535	0.27	18.9	17
Re_2B	$C2/m$	calc							394	192	2.05	496	0.29	15.7	17
ReB	$P\bar{6}m2$	calc							359	249	0.22	607	0.22	29.9	64
ReB	$P\bar{3}m1$	calc	618	168	171	915	248	225	352	254	1.39	614	0.21	31.7	17
Re_2B_3	$P6_3/mmc$	calc							351	264	1.33	633	0.20	34.4	64
ReB_2	$P6_3/mmc$	calc	636	156	126	1010	259	240	344	276	1.24	654	0.18	38.5	this work
	$P6_3/mmc$	calc	668	137	147	1063	273	266	362	294	1.23	693	0.18	40.4	9
	$P6_3/mmc$	calc	716	151	133	1108	290	283	375	314	1.19	736	0.17	44.0	10
	$P6_3/mmc$	calc	641	159	128	1037	271	241	350	284	1.23	670	0.18	39.6	11
	$P6_3/mmc$	calc	701	151	126	1089	282	275	366	307	1.19	719	0.17	43.3	12
	$P6_3/mmc$	expt							360					30.1(1.30)−48.0(5.6)	6
	$P6_3/mmc$	expt							173(4)	169(1)	1.02	382(3)	0.097(6)	20	13
	$P6_3/mmc$	expt−single-crystal	674	192	185	1023	269	241	383	273	1.40	661	0.21	39.5(2.5)	14
	$P6_3/mmc$	expt−powder	474	108			183		230	183	1.26	434	0.19	27.0(4.7)	14
ReB_3	$P\bar{6}m2$	calc	566	126	175	884	219	220	330	234	1.41	568	0.21	29.6	this work
	$P\bar{6}m2$	expt							306(5)			496(44)		34(3)	this work
	$P\bar{6}m2$	calc	575	140	181	911	223	218	341	237	1.44	576	0.22	29.0	17
	$P\bar{6}m2$	calc	567	130	175	905	229	219	333	239	1.39	579	0.21	30.4	18
ReB_4	$P6_3/mmc$	calc	568	122	123	999	173	223	319	232	1.38	560	0.21	30.3	this work
	$P6_3/mmc$	expt							281(4)			496(44)		34(3)	this work
ReB_4	$R\bar{3}m$	calc	557	116	137	977	186	221	319	232	1.38	560	0.21	30.3	20
	$R\bar{3}m$	calc	556	111	126	996	194	223	315	238	1.32	571	0.20	32.5	21
	$C2/m$	calc							303	234	1.29	558	0.19	33.0	17
ReB_5	P-6$m2$	calc	553	89	151	925	143	232	313	213	1.47	521	0.22	26.4	this work
ReB_6	$P6_3/mmc$	calc	551	103	121	970	145	224	307	218	1.41	528	0.21	28.2	this work
γ-B	$Pnnm$	calc							224	236	0.95	524	0.11	49	66
	$Pnnm$	calc							232	249	0.93	550	0.10	42.1	67
	$Pnnm$	expt							213.9(2.3)	227.2(9)	0.94	503.3	0.11	30.3	68

[a]For the sake of self-consistency between literature values, H_V were recalculated according Chen's empirical model[69] using reported B and G values.

https://doi.org/10.1021/acs.chemmater.2c00520
Chem. Mater. 2022, 34, 8138−8152

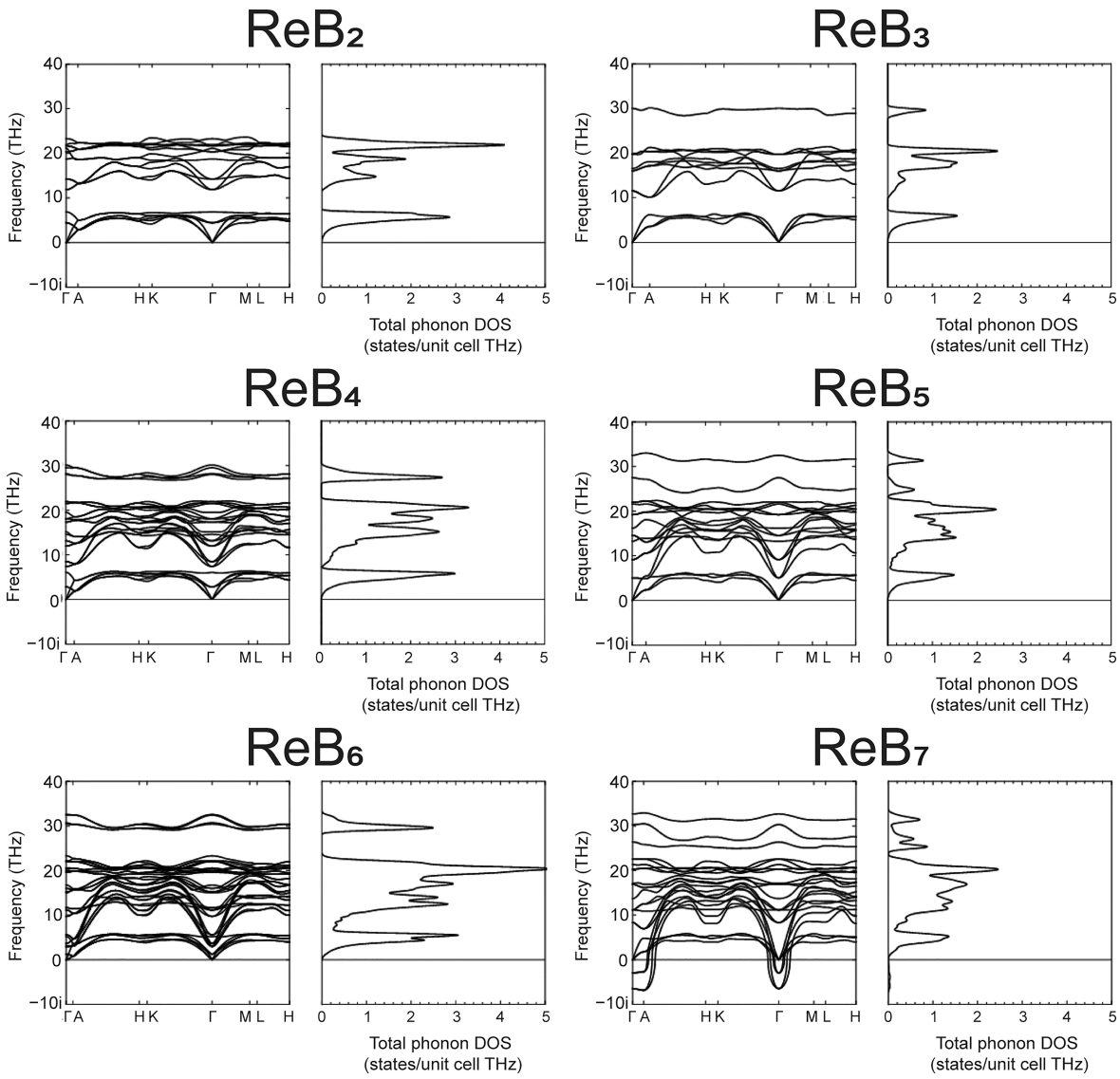

Figure 5. Phonon dispersion relations and phonon density of states (DOS) at ambient pressure calculated in the harmonic approximation for ReB_x phases (x = 2−7).

consists of such stacked layers and has a simple $P6_3/mmc$ crystal structure (Table S4). Even though the *hP6*-B becomes stable against γ-B at about 200 GPa, ζ-(α-Ga type) still remains lower in enthalpy to at least 550 GPa (Figure S7). At ambient conditions *hP6*-B would have a density of 2.81 g/cm^3, which is 11% higher than that of γ-B (2.53 g/cm^3, refs 74 and 75) and equal to ζ-(α-Ga type) boron (2.81 g/cm^3, ref 76).

We cannot fully exclude the possibility that crystal structures of ReB_x (x > 4) based on different principle(s) of structural organization would be more thermodynamically stable, but a detailed study on the stability and crystal structure of rhenium borides is out of the scope of the current work. It also should be noted that a decrease in the Re:B ratio will likely favor formation of boron clusters at some point. Structures where metal atoms occupy the voids of 3D cages formed by the interconnected boron clusters are found in many MB_x ($x \geq 4$) compounds (see ref 8 and references therein). However, the effects of the Re:B ratio, pressure, and temperature on the possible formation of boron clusters in rhenium borides are unclear at the moment, and therefore, investigation on these properties is reserved for further studies.

3.4. Mechanical Properties. The measured nanoindentation hardness of a mixture of ReB_3 and ReB_4 is 33.6(2.9) GPa (Figure S3). Using elastic constants derived from theory, we calculated bulk (B), shear (G), and Young's (E) moduli, Poisson's ratio (σ), and B/G for ReB_2 (x = 2−6) based on the Voigt−Reuss−Hill approximation.[77] Vickers hardness (H_V) values were estimated according to Chen's model:[69] $H_V = 2(k^2G)^{0.585} - 3$, where $k = G/B$ is Pugh's ratio. The estimated values compare well to our experiment (see Table 2), indicating that the use of Chen's model is reasonable for the studied systems. Therefore, similar estimations of the hardness based on the calculated elastic moduli were done for other rhenium borides found in the literature and for pure rhenium and γ-boron (see values in Table 2; variation of B, G, E, and H_V as a function of Re content is shown in Figure 7). The B/G value is employed in theoretical calculations to analyze ductility/brittleness of a material; an empirical border between these characteristics is often set to 1.75 (i.e., ductile materials are expected to have a B/G above 1.75 and brittle ones, below 1.75).[78] Based on this approach, all ReB_x compounds (x = 2−7) should be brittle, agreeing with their crystal structures

https://doi.org/10.1021/acs.chemmater.2c00520
Chem. Mater. 2022, 34, 8138−8152

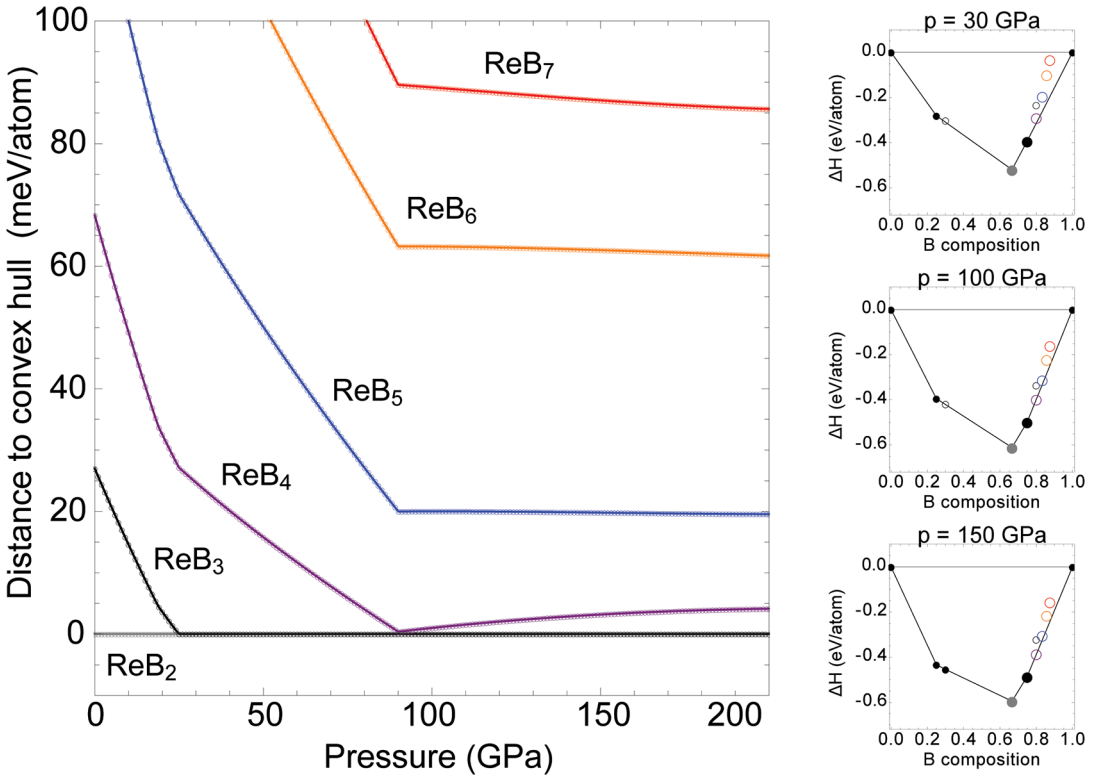

Figure 6. (Left) Distance to the convex hull of ReB_x (x = 2−7) phases as a function of pressure up to 200 GPa. ReB_3 becomes a stable phase at 25 GPa, ReB_4 is stable at 92 GPa, and ReB_5, ReB_6, and ReB_7 are above the convex hull at all considered pressures. (Right) Convex hull plots at pressures of 30, 100, and 150 GPa. Open circles are metastable phases, and filled circles are stable phases sitting on the convex hull. As a guide to the eye, the most relevant ReB_x (x = 2−7) phases are given by larger circles and are colored in accordance with the left image.

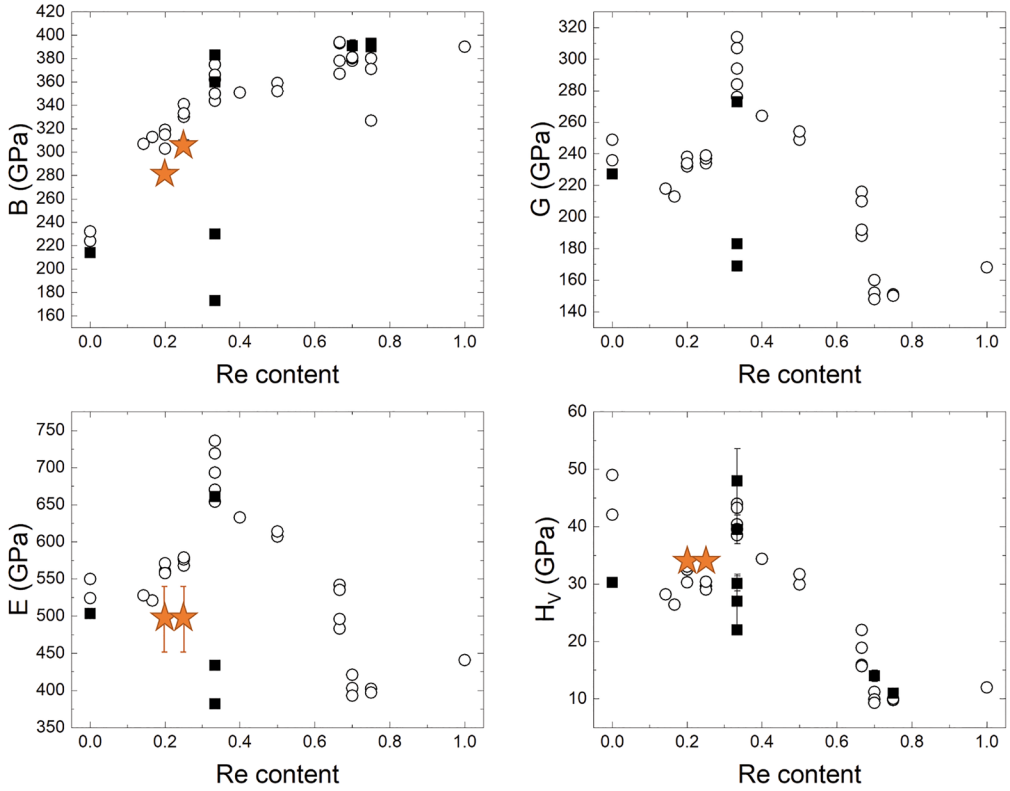

Figure 7. Variation of bulk (K), shear (G), and Young's (E) moduli and Vickers hardness (H_V) with rhenium content in the borides. Open symbols correspond to calculated values; solid symbols, to experimental ones. Black symbols correspond to literature values; orange stars, to values derived for a particle containing both ReB_3 and ReB_4.

https://doi.org/10.1021/acs.chemmater.2c00520
Chem. Mater. 2022, 34, 8138−8152

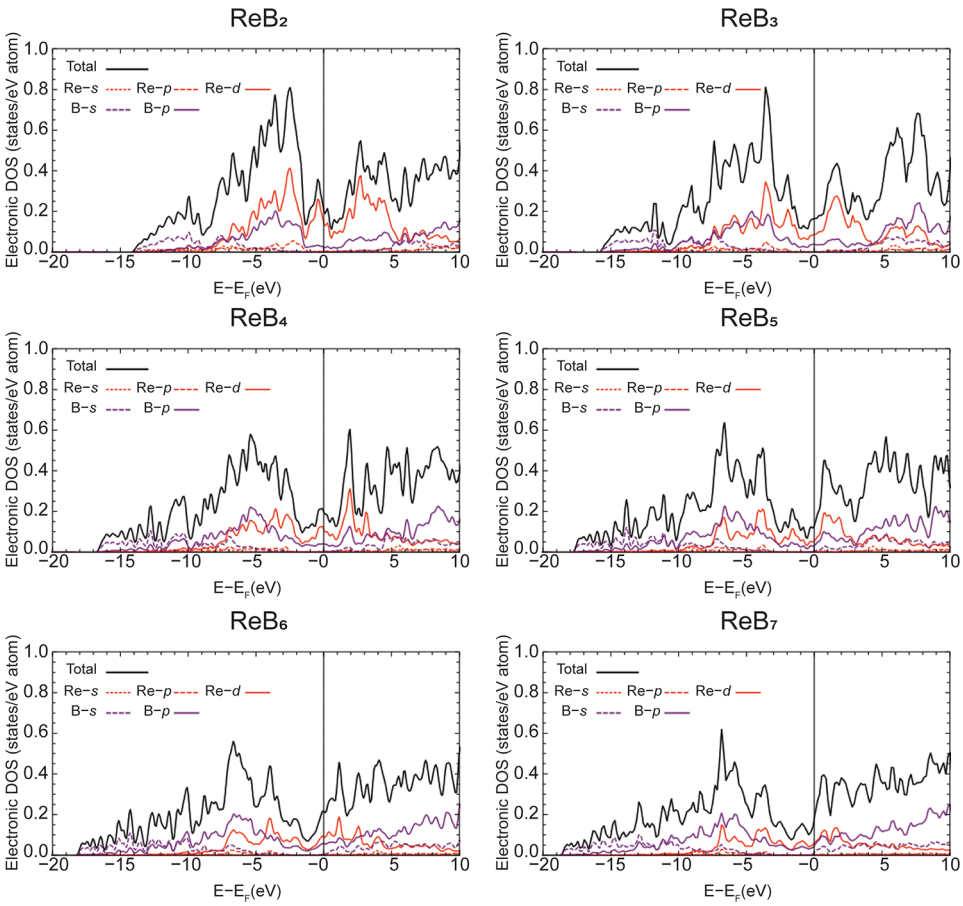

Figure 8. Calculated electronic DOS of ReB_x (x = 2−7) at ambient pressure. Energies are presented with respect to the Fermi energy of each compound. Black solid lines are the total DOS, while red and purple are for Re and B, respectively. Explanations for the partial s-, p-, and d-orbital contributions are given in the legends.

featuring strong covalent bonds. Another measure of the degree of covalent bonding is the Poisson ratio (σ), defined as a negative of the ratio between transverse and longitudinal strain under uniaxial stress. The Poisson ratio slightly increases from 0.18 for ReB_2 to 0.22 for ReB_6 due to the increase of strong B−B bonds in the crystal structure.

All boron-rich borides are highly incompressible (B > 270 GPa), while bulk moduli monotonically increase with an increase in rhenium content (Figure 7). Although the bulk modulus itself determines resistance of the material to the isotropic compression, a higher bulk modulus would not single-handedly result in higher hardness. The second and even more important characteristic is the ability of the material to resist shear stresses, which is characterized by the shear modulus G. The rhenium-content dependence of G (E and H_V as well) is not monotonic: it has two maxima, namely, at around ReB_2 and γ-B (Figure 7). While G, E, and H_V drop abruptly for Re_nB_{1-n} (n > 0.67), they remain relatively high for compositions with $n \leq 0.67$, suggesting fairly good mechanical properties for these compounds. Applying high pressures to the synthesis of boron-rich rhenium borides along with chemical doping can open a route to novel hard materials.

3.5. Electronic Properties of ReB_x. The electronic DOS has been calculated for all ReB_x compounds (x = 2−7) at ambient pressure and is presented in Figure 8. Electrical resistivity measurements show that ReB_3 and ReB_4 are metals. Our calculations confirm that all compounds have metallic electronic structure, owing to the finite DOS at E_F. Starting with ReB_2, there is a significant hybridization between Re-5d and B-2p states in the valence band. In fact, it survives in the conduction band. The hybridization between these two orbitals indicates strong covalent bonding. As B is more electronegative than Re, there is a charge transfer from Re to B, characteristic of ionic bonding, making the boron sublattice isoelectronic to neutral carbon, at least in ReB_2. In the work of Robinson et al.,[79] bonding properties of different metal borides were investigated theoretically. They noted how a metal that is too covalent with boron negatively affects incompressibility of the metal boride, and a metal that is too ionic with boron lowers the shear strength. It is concluded that Re in ReB_2 provides the perfect electron count to balance covalent and ionic behavior, akin to its superhardness. Furthermore, the overlap between Re-5d and B-2p remains in all ReB_x compounds. The overall shape of the DOS below E_F is the same for all boron concentrations, with the most noticeable difference being the deepest valence states, dominated by B-2s, getting shifted downward upon further addition of boron. Moreover, as one could expect, it is apparent that Re contributes less to the total DOS as the boron concentration increases.

There is a peak in the DOS of ReB_2 at E_F, mainly consisting of Re-5d states. This type of peak was also seen in the work of Alling et al.[80] in the related 3d metal diboride TiB_2. Symmetry projection of Ti d-states in TiB_2 revealed that this feature mainly comes from $3d_{z^2}$ and $3d_{x^2-y^2}$ states, and it even survives in pure hexagonal Ti. If ReB_2 is understood within a rigid band

https://doi.org/10.1021/acs.chemmater.2c00520
Chem. Mater. 2022, 34, 8138−8152

model, with three additional electrons, it is therefore indicative that this peak in the DOS is due to Re 5d−5d hybridization in the *c*-direction. As more boron is added between the hexagonal Re layers, this hybridization likely weakens. Nevertheless, from the viewpoint of an electronic structure, the general resemblance of the boron-rich ReB_x phases suggests they should have mechanical properties comparable to ReB_2.

Interestingly, the DOS of ReB_2 shows a higher peak at E_F than those of the ReB_x despite the fact that the former is the most stable phase at ambient pressure. One could argue that the one-electron contribution to the total energy determined by the DOS should favor structures with higher B content. However, this is only one contribution to the total energy, which also includes other terms. One-electron energy often dominates phase stability of different polymorphs for materials with metallic bonding. However, it is often insufficient for a discussion of relative stability of phases with different compositions and complex chemical bonding, discussed for Re borides above. Moreover, one should remember that electronic states around the Fermi energy are of Re character, and their contribution to the total DOS calculated per atom gradually decreases due to an increase of the boron relative content. Furthermore, the instability of greater boron rich compositions at ambient pressure is related to energetics of the boron−boron bonds that are not reflected by the DOS around the Fermi level. The calculations of the enthalpy employed for quantitative analysis of the phase stability in Figure 6 include all the contributions to the total energy, as well as the *PV* term.

4. CONCLUSIONS

We report successful syntheses of ReB_3 and ReB_4, two borides with the highest boron contents in the Re−B system. Their crystal structures determined by single-crystal X-ray diffraction demonstrate striking similarities with well-known hard ReB_2, where hexagonal sheets of rhenium atoms interchange with layers formed by puckered six-membered rings of boron in the chair conformation. The new compounds possess short incompressible Re−B and B−B bonds oriented along *c*-axes, which result in anisotropy in axial compressibility, elastic tensor constants, and mechanical behavior.

We postulate the existence of borides with even higher boron contents such as ReB_5, ReB_6, and ReB_7 that might be organized by the same principle as ReB_x (x = 2−4) and be stabilized at high pressures. The synthesized and proposed borides can be described as intercalated compounds where rhenium atoms in close-packed layers are located between the fragments of an inferred ultradense *hP6*-boron network.

Our study demonstrated the advantages of using single-crystal XRD diffraction at high-pressure studies in DACs. The method can be applied as an ultimate chemical probe for fast screening of the compositional space at specific pressures and temperatures. The derived *PT* conditions of synthesis in DACs can then be used for the scale-up synthesis of the novel promising compounds in a large-volume apparatus.

■ ASSOCIATED CONTENT

Supporting Information

The Supporting Information is available free of charge at https://pubs.acs.org/doi/10.1021/acs.chemmater.2c00520.

Additional experimental details and data, such as photographs of the setup, SEM, hardness, resistance measurements, details of high-pressure high-temperature synthesis, crystallographic information, details of theoretical calculations (PDF)

Crystallographic data for ReB_3 at ambient and high pressure (CIF)

Crystallographic data for ReB_4 at ambient and high pressure (CIF)

■ AUTHOR INFORMATION

Corresponding Author

Elena Bykova − *Earth and Planets Laboratory, Carnegie Institution for Science, Washington, D.C. 20015, United States; Bayerisches Geoinstitut, University of Bayreuth, 95440 Bayreuth, Germany;* orcid.org/0000-0001-8652-024X; Email: knilav@gmail.com

Authors

Erik Johansson − *Department of Physics, Chemistry and Biology (IFM), Linköping University, SE-58183 Linköping, Sweden*

Maxim Bykov − *Earth and Planets Laboratory, Carnegie Institution for Science, Washington, D.C. 20015, United States; Institute of Inorganic Chemistry, University of Cologne, 50939 Cologne, Germany;* orcid.org/0000-0003-0248-1728

Stella Chariton − *Center for Advanced Radiation Sources, The University of Chicago, Chicago, Illinois 60637, United States;* orcid.org/0000-0001-5522-0498

Hongzhan Fei − *Bayerisches Geoinstitut, University of Bayreuth, 95440 Bayreuth, Germany*

Sergey V. Ovsyannikov − *Bayerisches Geoinstitut, University of Bayreuth, 95440 Bayreuth, Germany;* orcid.org/0000-0003-1027-0998

Alena Aslandukova − *Bayerisches Geoinstitut, University of Bayreuth, 95440 Bayreuth, Germany*

Stefan Gabel − *Materials Science and Engineering, Institute I, Interdisciplinary Center for Nanostructured Films (IZNF), Friedrich-Alexander-Universität Erlangen-Nürnberg, D-91058 Erlangen, Germany*

Hendrik Holz − *Materials Science and Engineering, Institute I, Interdisciplinary Center for Nanostructured Films (IZNF), Friedrich-Alexander-Universität Erlangen-Nürnberg, D-91058 Erlangen, Germany; Institute of Materials Engineering, University of Kassel, 34125 Kassel, Germany*

Benoit Merle − *Materials Science and Engineering, Institute I, Interdisciplinary Center for Nanostructured Films (IZNF), Friedrich-Alexander-Universität Erlangen-Nürnberg, D-91058 Erlangen, Germany; Institute of Materials Engineering, University of Kassel, 34125 Kassel, Germany*

Björn Alling − *Department of Physics, Chemistry and Biology (IFM), Linköping University, SE-58183 Linköping, Sweden*

Igor A. Abrikosov − *Department of Physics, Chemistry and Biology (IFM), Linköping University, SE-58183 Linköping, Sweden*

Jesse S. Smith − *HPCAT, X-ray Science Division, Argonne National Laboratory, Argonne, Illinois 60439, United States*

Vitali B. Prakapenka − *Center for Advanced Radiation Sources, The University of Chicago, Chicago, Illinois 60637, United States;* orcid.org/0000-0001-9270-2330

Tomoo Katsura − *Bayerisches Geoinstitut, University of Bayreuth, 95440 Bayreuth, Germany*

Natalia Dubrovinskaia − *Department of Physics, Chemistry and Biology (IFM), Linköping University, SE-58183 Linköping, Sweden; Material Physics and Technology at*

Extreme Conditions, Laboratory of Crystallography, University of Bayreuth, 95440 Bayreuth, Germany

Alexander F. Goncharov − *Earth and Planets Laboratory, Carnegie Institution for Science, Washington, D.C. 20015, United States*

Leonid Dubrovinsky − *Bayerisches Geoinstitut, University of Bayreuth, 95440 Bayreuth, Germany*

Complete contact information is available at:
https://pubs.acs.org/10.1021/acs.chemmater.2c00520

Notes

The authors declare no competing financial interest.

■ ACKNOWLEDGMENTS

E.B. and A.F.G. acknowledge support from the Carnegie Institution of Washington. E.B. acknowledges financial support from the program 'Promotion of Equal Opportunities for Women in Research and Teaching' funded by the Free State of Bavaria. M.B. acknowledges the support of Deutsche Forschungsgemeinschaft (DFG project BY112/2-1). Portions of this work were performed at GeoSoilEnviroCARS (The University of Chicago, Sector 13), Advanced Photon Source (APS), Argonne National Laboratory. GeoSoilEnviroCARS is supported by the National Science Foundation - Earth Sciences (EAR-1634415) and Department of Energy - GeoSciences (DE-FG02-94ER14466). This research used resources of the Advanced Photon Source, a U.S. Department of Energy (DOE) Office of Science User Facility operated for the DOE Office of Science by Argonne National Laboratory under Contract No. DE-AC02-06CH11357. Portions of this work were performed at HPCAT (Sector 16), Advanced Photon Source (APS), Argonne National Laboratory. HPCAT operations are supported by DOE-NNSA's Office of Experimental Sciences. This research used resources from the Center for Nanoanalysis and Electron Microscopy (CENEM) at Friedrich-Alexander University Erlangen-Nürnberg. The contribution of B.M., S.G., and H.H. to this project has received funding from the European Research Council (ERC) under the European Union's Horizon 2020 research and innovation programme (grant agreement No. 949626). We thank Dorothea Wiesner for the help with SEM measurements and Raphael Njul for SEM sample preparation. All calculations were performed using supercomputer resources provided by the Swedish National Infrastructure for Computing (SNIC) at the National Supercomputer Centre (NSC). Financial support from the Knut and Alice Wallenberg (KAW) Foundation, through project grant number KAW 2015.0043 is greatly acknowledged. We acknowledge financial support from the Swedish Research Council (VR) through International Career Grant No. 2014-6336, Grant No. 2019-05403, and Grant No. 2019-05600, from the Swedish Government Strategic Research Areas in Materials Science on Functional Materials at Linköping University (Faculty Grant SFO-Mat-LiU No. 2009 00971), from Marie Sklodowska Curie Actions, Cofund, Project INCA 600398, and from the Knut and Alice Wallenberg Foundation (Wallenberg Scholar Grant No. KAW-2018.0194), as well as support from the Swedish Foundation for Strategic Research through the Future Research Leaders 6 program, FFL 15-0290. This study is also supported by the European Research Council (ERC) under the European Union's Horizon 2020 research and innovation program (proposal no. 787 527).

■ REFERENCES

(1) Nagamatsu, J.; Nakagawa, N.; Muranaka, T.; Zenitani, Y.; Akimitsu, J. Superconductivity at 39 K in Magnesium Diboride. *Nature* **2001**, *410* (6824), 63−64.

(2) Cumberland, R. W.; Weinberger, M. B.; Gilman, J. J.; Clark, S. M.; Tolbert, S. H.; Kaner, R. B. Osmium Diboride, an Ultra-Incompressible, Hard Material. *J. Am. Chem. Soc.* **2005**, *127* (20), 7264−7265.

(3) Mohammadi, R.; Lech, A. T.; Xie, M.; Weaver, B. E.; Yeung, M. T.; Tolbert, S. H.; Kaner, R. B. Tungsten Tetraboride, an Inexpensive Superhard Material. *Proc. Natl. Acad. Sci. U. S. A.* **2011**, *108* (27), 10958−10962.

(4) Mohammadi, R.; Xie, M.; Lech, A. T.; Turner, C. L.; Kavner, A.; Tolbert, S. H.; Kaner, R. B. Toward Inexpensive Superhard Materials: Tungsten Tetraboride-Based Solid Solutions. *J. Am. Chem. Soc.* **2012**, *134* (51), 20660−20668.

(5) Gou, H.; Dubrovinskaia, N.; Bykova, E.; Tsirlin, A. A.; Kasinathan, D.; Schnelle, W.; Richter, A.; Merlini, M.; Hanfland, M.; Abakumov, A. M.; Batuk, D.; Van Tendeloo, G.; Nakajima, Y.; Kolmogorov, A. N.; Dubrovinsky, L. Discovery of a Superhard Iron Tetraboride Superconductor. *Phys. Rev. Lett.* **2013**, *111* (15), 157002.

(6) Chung, H.-Y. Y.; Weinberger, M. B.; Levine, J. B.; Kavner, A.; Yang, J.-M. M.; Tolbert, S. H.; Kaner, R. B. Synthesis of Ultra-Incompressible Superhard Rhenium Diboride at Ambient Pressure. *Science* **2007**, *316* (5823), 436−439.

(7) Akopov, G.; Yeung, M. T.; Kaner, R. B. Rediscovering the Crystal Chemistry of Borides. *Adv. Mater.* **2017**, *29* (21), 1604506.

(8) Albert, B.; Hofmann, K. Metal Borides: Versatile Structures and Properties. *Handb. Solid State Chem.* **2017**, 435−453.

(9) Hao, X.; Xu, Y.; Wu, Z.; Zhou, D.; Liu, X.; Cao, X.; Meng, J. Low-Compressibility and Hard Materials Re B2 and W B2: Prediction from First-Principles Study. *Phys. Rev. B - Condens. Matter Mater. Phys.* **2006**, *74* (22), 1−5.

(10) Liang, Y.; Zhang, B. Mechanical and Electronic Properties of Superhard Re B2. *Phys. Rev. B - Condens. Matter Mater. Phys.* **2007**, *76* (13), 3−6.

(11) Zhou, W.; Wu, H.; Yildirim, T. Electronic, Dynamical, and Thermal Properties of Ultra-Incompressible Superhard Rhenium Diboride: A Combined First-Principles and Neutron Scattering Study. *Phys. Rev. B - Condens. Matter Mater. Phys.* **2007**, *76* (18), 1−6.

(12) Zhu, X.; Li, D.; Cheng, X. Elasticity Properties of the Low-Compressible Material ReB2. *Solid State Commun.* **2008**, *147* (7−8), 301−304.

(13) Qin, J.; He, D.; Wang, J.; Fang, L.; Lei, L.; Li, Y.; Hu, J.; Kou, Z.; Bi, Y. Is Rhenium Diboride a Superhard Material. *Adv. Mater.* **2008**, *20* (24), 4780−4783.

(14) Levine, J. B.; Betts, J. B.; Garrett, J. D.; Guo, S. Q.; Eng, J. T.; Migliori, A.; Kaner, R. B. Full Elastic Tensor of a Crystal of the Superhard Compound ReB2. *Acta Mater.* **2010**, *58* (5), 1530−1535.

(15) Aronsson, B.; Stenberg, E.; Åselius, J.; Refn, S.; Westin, G. Borides of Rhenium and the Platinum Metals. The Crystal Structure of Re7B3, ReB3, Rh7B3, RhB ∼ 1.1, IrB ∼ 1.1 and PtB. *Acta Chem. Scand.* **1960**, *14*, 733−741.

(16) La Placa, S. J.; Post, B. The Crystal Structure of Rhenium Diboride. *Acta Crystallogr.* **1962**, *15* (2), 97−99.

(17) Zhao, X.; Nguyen, M. C.; Wang, C.-Z.; Ho, K.-M. New Stable Re−B Phases for Ultra-Hard Materials. *J. Phys.: Condens. Matter* **2014**, *26* (45), 455401.

(18) Yan, Q.; Wang, Y. X.; Wang, B.; Yang, J.; Yang, G. The Ground-State Structure and Physical Properties of ReB3 and IrB3 Predicted from First Principles. *RSC Adv.* **2015**, *5* (33), 25919−25928.

(19) Wang, M.; Li, Y.; Cui, T.; Ma, Y.; Zou, G. Origin of Hardness in WB4 and Its Implications for ReB 4, TaB4, MoB4, TcB4, and OsB 4. *Appl. Phys. Lett.* **2008**, *93* (10), 25−28.

(20) Wang, B.; Wang, D. Y.; Wang, Y. X. A New Hard Phase of ReB4 Predicted from First Principles. *J. Alloys Compd.* **2013**, *573*, 20−26.

(21) Ma, J.; Wu, Y.; Fu, Z.; Wei, Q.; Yang, Z.; Gao, J.; Zhou, J. Structural, Mechanical, and Thermodynamic Properties of R-3m ReB4 under High Pressure. *Eur. Phys. J. B* **2019**, *92* (9), 206.
(22) Parakhonskiy, G.; Dubrovinskaia, N.; Bykova, E.; Wirth, R.; Dubrovinsky, L. Experimental Pressure-Temperature Phase Diagram of Boron: Resolving the Long-Standing Enigma. *Sci. Rep.* **2011**, *1*, 96.
(23) Letoullec, R.; Pinceaux, J. P.; Loubeyre, P. The Membrane Diamond Anvil Cell: A New Device for Generating Continuous Pressure and Temperature Variations. *High Press. Res.* **1988**, *1* (1), 77−90.
(24) Fei, Y.; Ricolleau, A.; Frank, M.; Mibe, K.; Shen, G.; Prakapenka, V. Toward an Internally Consistent Pressure Scale. *Proc. Natl. Acad. Sci. U. S. A.* **2007**, *104* (22), 9182−9186.
(25) Prakapenka, V. B.; Kubo, A.; Kuznetsov, A.; Laskin, A.; Shkurikhin, O.; Dera, P.; Rivers, M. L.; Sutton, S. R. Advanced Flat Top Laser Heating System for High Pressure Research at GSECARS: Application to the Melting Behavior of Germanium. *High Press. Res.* **2008**, *28* (3), 225−235.
(26) Heinz, D. L.; Jeanloz, R. Temperature Measurements in the Laser-Heated Diamond Cell. In *High-Pressure Research in Mineral Physics: A Vol. in Honor of Syun-iti Akimoto*, Vol. *39*; Manghnani, M. H., Syono, Y., Eds.; Terra Scientific Publishing, 1987; pp 113−127, DOI: 10.1029/GM039p0113.
(27) Prescher, C.; Prakapenka, V. B. DIOPTAS: A Program for Reduction of Two-Dimensional X-Ray Diffraction Data and Data Exploration. *High Press. Res.* **2015**, *35* (3), 223−230.
(28) Hrubiak, R.; Smith, J. S.; Shen, G. Multimode Scanning X-Ray Diffraction Microscopy for Diamond Anvil Cell Experiments. *Rev. Sci. Instrum.* **2019**, *90* (2), 025109.
(29) Petříček, V.; Dušek, M.; Palatinus, L. Crystallographic Computing System JANA2006: General Features. *Zeitschrift für Krist. - Cryst. Mater.* **2014**, *229* (5), 345−352.
(30) *CrysAlisPro Software System, version 1.171.40.84a*; Rigaku Oxford Diffraction: Oxford, UK, 2019.
(31) Sheldrick, G. M. SHELXT − Integrated Space-Group and Crystal-Structure Determination. *Acta Crystallogr. Sect. A Found. Adv.* **2015**, *71* (1), 3−8.
(32) Sheldrick, G. M. Crystal Structure Refinement with SHELXL. *Acta Crystallogr. Sect. C Struct. Chem.* **2015**, *71* (1), 3−8.
(33) Dolomanov, O. V.; Bourhis, L. J.; Gildea, R. J.; Howard, J. A. K.; Puschmann, H. OLEX2 : A Complete Structure Solution, Refinement and Analysis Program. *J. Appl. Crystallogr.* **2009**, *42* (2), 339−341.
(34) Frost, D.; Poe, B.; Trønnes, R.; Liebske, C.; Duba, A.; Rubie, D. A New Large-Volume Multianvil System. *Phys. Earth Planet. Inter.* **2004**, *143−144*, 507−514.
(35) Ovsyannikov, S. V.; Bykov, M.; Bykova, E.; Kozlenko, D. P.; Tsirlin, A. A.; Karkin, A. E.; Shchennikov, V. V.; Kichanov, S. E.; Gou, H.; Abakumov, A. M.; Egoavil, R.; Verbeeck, J.; McCammon, C.; Dyadkin, V.; Chernyshov, D.; van Smaalen, S.; Dubrovinsky, L. S. Charge-Ordering Transition in Iron Oxide Fe4O5 Involving Competing Dimer and Trimer Formation. *Nat. Chem.* **2016**, *8* (5), 501−508.
(36) Ishii, T.; Shi, L.; Huang, R.; Tsujino, N.; Druzhbin, D.; Myhill, R.; Li, Y.; Wang, L.; Yamamoto, T.; Miyajima, N.; Kawazoe, T.; Nishiyama, N.; Higo, Y.; Tange, Y.; Katsura, T. Generation of Pressures over 40 GPa Using Kawai-Type Multi-Anvil Press with Tungsten Carbide Anvils. *Rev. Sci. Instrum.* **2016**, *87* (2), 1−8.
(37) Merle, B.; Maier-Kiener, V.; Pharr, G. M. Influence of Modulus-to-Hardness Ratio and Harmonic Parameters on Continuous Stiffness Measurement during Nanoindentation. *Acta Mater.* **2017**, *134*, 167−176.
(38) Oliver, W. C.; Pharr, G. M. An Improved Technique for Determining Hardness and Elastic Modulus Using Load and Displacement Sensing Indentation Experiments. *J. Mater. Res.* **1992**, *7* (6), 1564−1583.
(39) Oliver, W. C.; Pharr, G. M. Measurement of Hardness and Elastic Modulus by Instrumented Indentation: Advances in Understanding and Refinements to Methodology. *J. Mater. Res.* **2004**, *19* (1), 3−20.
(40) Hohenberg, P.; Kohn, W. Inhomogeneous Electron Gas. *Phys. Rev.* **1964**, *136* (3B), B864−B871.
(41) Kohn, W.; Sham, L. J. Self-Consistent Equations Including Exchange and Correlation Effects. *Phys. Rev.* **1965**, *140* (4A), A1133−A1138.
(42) Ceperley, D. M.; Alder, B. J. Ground State of the Electron Gas by a Stochastic Method. *Phys. Rev. Lett.* **1980**, *45* (7), 566−569.
(43) Perdew, J. P.; Zunger, A. Self-Interaction Correction to Density-Functional Approximations for Many-Electron Systems. *Phys. Rev. B* **1981**, *23* (10), 5048−5079.
(44) Kresse, G.; Furthmüller, J. Efficient Iterative Schemes for Ab Initio Total-Energy Calculations Using a Plane-Wave Basis Set. *Phys. Rev. B* **1996**, *54* (16), 11169−11186.
(45) Kresse, G.; Joubert, D. From Ultrasoft Pseudopotentials to the Projector Augmented-Wave Method. *Phys. Rev. B* **1999**, *59* (3), 1758−1775.
(46) Blöchl, P. E. Projector Augmented-Wave Method. *Phys. Rev. B* **1994**, *50* (24), 17953−17979.
(47) Perdew, J. P.; Burke, K.; Ernzerhof, M. Generalized Gradient Approximation Made Simple. *Phys. Rev. Lett.* **1996**, *77* (18), 3865−3868.
(48) Monkhorst, H. J.; Pack, J. D. Special Points for Brillouin-Zone Integrations. *Phys. Rev. B* **1976**, *13* (12), 5188−5192.
(49) Togo, A.; Tanaka, I. First Principles Phonon Calculations in Materials Science. *Scr. Mater.* **2015**, *108*, 1−5.
(50) Parlinski, K.; Li, Z. Q.; Kawazoe, Y. First-Principles Determination of the Soft Mode in Cubic ZrO2. *Phys. Rev. Lett.* **1997**, *78* (21), 4063−4066.
(51) Birch, F. Finite Elastic Strain of Cubic Crystals. *Phys. Rev.* **1947**, *71* (11), 809−824.
(52) Murnaghan, F. D. The Compressibility of Media under Extreme Pressures. *Proc. Natl. Acad. Sci. U. S. A.* **1944**, *30* (9), 244−247.
(53) Katsura, T.; Tange, Y. A Simple Derivation of the Birch−Murnaghan Equations of State (EOSs) and Comparison with EOSs Derived from Other Definitions of Finite Strain. *Minerals* **2019**, *9* (12), 745.
(54) Blöchl, P. E.; Jepsen, O.; Andersen, O. K. Improved Tetrahedron Method for Brillouin-Zone Integrations. *Phys. Rev. B* **1994**, *49* (23), 16223−16233.
(55) Ektarawong, A.; Simak, S. I.; Hultman, L.; Birch, J.; Tasnádi, F.; Wang, F.; Alling, B. Effects of Configurational Disorder on the Elastic Properties of Icosahedral Boron-Rich Alloys Based on B 6 O, B 13 C 2, and B 4 C, and Their Mixing Thermodynamics. *J. Chem. Phys.* **2016**, *144* (13), 134503.
(56) Tasnádi, F.; Odén, M.; Abrikosov, I. A. Ab Initio Elastic Tensor of Cubic Ti 0.5 Al 0.5 N Alloys: Dependence of Elastic Constants on Size and Shape of the Supercell Model and Their Convergence. *Phys. Rev. B* **2012**, *85* (14), 144112.
(57) Golesorkhtabar, R.; Pavone, P.; Spitaler, J.; Puschnig, P.; Draxl, C. ElaStic: A Tool for Calculating Second-Order Elastic Constants from First Principles. *Comput. Phys. Commun.* **2013**, *184* (8), 1861−1873.
(58) Nye, J. F. *Physical Properties of Crystals: Their Representation by Tensors and Matrices*; Clarendon Press: Oxford, 1985.
(59) Mouhat, F.; Coudert, F.-X. Necessary and Sufficient Elastic Stability Conditions in Various Crystal Systems. *Phys. Rev. B* **2014**, *90* (22), 224104.
(60) Zhang, M.; Wang, H.; Wang, H.; Cui, T.; Ma, Y. Structural Modifications and Mechanical Properties of Molybdenum Borides from First Principles. *J. Phys. Chem. C* **2010**, *114* (14), 6722−6725.
(61) Jamieson, J. C. Crystal Structures Adopted by Black Phosphorus at High Pressures. *Science* **1963**, *139* (3561), 1291−1292.
(62) Burrage, K. C.; Lin, C.-M.; Chen, W.-C.; Chen, C.-C.; Vohra, Y. K. Experimental and Computational Studies on Superhard Material Rhenium Diboride under Ultrahigh Pressures. *Materials (Basel)* **2020**, *13* (7), 1657.

(63) Neun, C.; Petermüller, B.; Bayarjargal, L.; Morgenroth, W.; Avalos-Borja, M.; Silva-Pereyra, H. G.; Spahr, D.; Schmuck, F.; Milman, V.; Huppertz, H.; Winkler, B. Compressibility, Microcalorimetry, Elastic Properties and EELS of Rhenium Borides. *Solid State Sci.* **2018**, *81*, 71−81.
(64) Gou, H.; Wang, Z.; Zhang, J.; Yan, S.; Gao, F. Structural Stability and Elastic and Electronic Properties of Rhenium Borides: First Principle Investigations. *Inorg. Chem.* **2009**, *48* (2), 581−587.
(65) Bannikov, V. V.; Shein, I. R.; Ivanovskii, A. L. Elastic and Electronic Properties of Hexagonal Rhenium Sub-Nitrides Re. *Phys. Status Solidi* **2011**, *248* (6), 1369.
(66) Jiang, C.; Lin, Z.; Zhang, J.; Zhao, Y. First-Principles Prediction of Mechanical Properties of Gamma-Boron. *Appl. Phys. Lett.* **2009**, *94* (19), 93−96.
(67) Aydin, S.; Simsek, M. First-Principles Calculations of Elemental Crystalline Boron Phases under High Pressure: Orthorhombic B28 and Tetragonal B48. *J. Alloys Compd.* **2011**, *509* (17), 5219−5229.
(68) Qin, J.; Nishiyama, N.; Ohfuji, H.; Shinmei, T.; Lei, L.; He, D.; Irifune, T. Polycrystalline γ-Boron: As Hard as Polycrystalline Cubic Boron Nitride. *Scr. Mater.* **2012**, *67* (3), 257−260.
(69) Chen, X. Q.; Niu, H.; Li, D.; Li, Y. Modeling Hardness of Polycrystalline Materials and Bulk Metallic Glasses. *Intermetallics* **2011**, *19* (9), 1275−1281.
(70) Migliori, A.; Ledbetter, H.; Leisure, R. G.; Pantea, C.; Betts, J. B. Diamond's Elastic Stiffnesses from 322 to 10 K. *J. Appl. Phys.* **2008**, *104* (5), 053512.
(71) Li, X.; Wang, H.; Lv, J.; Liu, Z. Phase Diagram and Physical Properties of Iridium Tetraboride from First Principles. *Phys. Chem. Chem. Phys.* **2016**, *18* (18), 12569−12575.
(72) Wang, Y.; Yao, T.; Wang, L. M.; Yao, J.; Li, H.; Zhang, J.; Gou, H. Structural and Relative Stabilities, Electronic Properties and Possible Reactive Routing of Osmium and Ruthenium Borides from First-Principles Calculations. *J. Chem. Soc. Dalt. Trans.* **2013**, *42* (19), 7041−7050.
(73) Kvashnin, A. G.; Zakaryan, H. A.; Zhao, C.; Duan, Y.; Kvashnina, Y. A.; Xie, C.; Dong, H.; Oganov, A. R. New Tungsten Borides, Their Stability and Outstanding Mechanical Properties. *J. Phys. Chem. Lett.* **2018**, *9* (12), 3470−3477.
(74) Solozhenko, V. L.; Kurakevych, O. O.; Oganov, A. R. On the Hardness of a New Boron Phase, Orthorhombic γ-B28. *J. Superhard Mater.* **2008**, *30* (6), 428−429.
(75) Zarechnaya, E. Y.; Dubrovinsky, L.; Dubrovinskaia, N.; Filinchuk, Y.; Chernyshov, D.; Dmitriev, V.; Miyajima, N.; El Goresy, A.; Braun, H. F.; Van Smaalen, S.; Kantor, I.; Kantor, A.; Prakapenka, V.; Hanfland, M.; Mikhaylushkin, A. S.; Abrikosov, I. A.; Simak, S. I. Superhard Semiconducting Optically Transparent High Pressure Phase of Boron. *Phys. Rev. Lett.* **2009**, *102* (18), 185501.
(76) Oganov, A. R.; Chen, J.; Gatti, C.; Ma, Y.; Ma, Y.; Glass, C. W.; Liu, Z.; Yu, T.; Kurakevych, O. O.; Solozhenko, V. L. Ionic High-Pressure Form of Elemental Boron. *Nature* **2009**, *457* (7231), 863−867.
(77) Hill, R. The Elastic Behaviour of a Crystalline Aggregate. *Proc. Phys. Soc. Sect. A* **1952**, *65* (5), 349−354.
(78) Pugh, S. F. Relations between the Elastic Moduli and the Plastic Properties of Polycrystalline Pure Metals. *London, Edinburgh, Dublin Philos. Mag. J. Sci.* **1954**, *45* (367), 823−843.
(79) Robinson, P. J.; Liu, G.; Ciborowski, S.; Martinez-Martinez, C.; Chamorro, J. R.; Zhang, X.; McQueen, T. M.; Bowen, K. H.; Alexandrova, A. N. Mystery of Three Borides: Differential Metal-Boron Bonding Governing Superhard Structures. *Chem. Mater.* **2017**, *29* (23), 9892−9896.
(80) Alling, B.; Högberg, H.; Armiento, R.; Rosen, J.; Hultman, L. A Theoretical Investigation of Mixing Thermodynamics, Age-Hardening Potential, and Electronic Structure of Ternary M11-XM2xB2 Alloys with AlB2 Type Structure. *Sci. Rep* **2015**, *5* (May), 1−7.

https://doi.org/10.1021/acs.chemmater.2c00520
Chem. Mater. 2022, 34, 8138−8152